Crumpled paper sheets: Low-cost biobased cellular materials for structural applications

F. Martoïa [a,*], L. Orgéas [a], P.J.J. Dumont [b], J.-F. Bloch [a], F. Flin [c], J. Viguié [d]

[a] Univ. Grenoble Alpes, CNRS, Grenoble INP, 3SR Lab, F-38000 Grenoble, France
[b] Univ. Lyon, INSA-Lyon, CNRS UMR 5259, LaMCoS, F-69621 Lyon, France
[c] Météo-France - CNRS, CNRM UMR 3589, CEN, F-38000 Grenoble, France
[d] Centre Technique du Papier (CTP), F-38000 Grenoble, France

HIGHLIGHTS

- Biobased porous materials with tunable porosity were obtained by crumpling and thermo-hygro-forming low-cost paper sheets.
- Tomographic images revealed that crumpled papers constitute a new class of porous materials with self-locked architecture.
- Crumpled papers exhibited a reproducible compression behavior between foams and entangled fibrous materials.
- Sheet curvature distributions revealed that the geometry of the folds was not affected by the thickness of initial sheets.
- Crumpled papers showed interesting specific mechanical properties between those of flexible and rigid polymer foams.

GRAPHICAL ABSTRACT
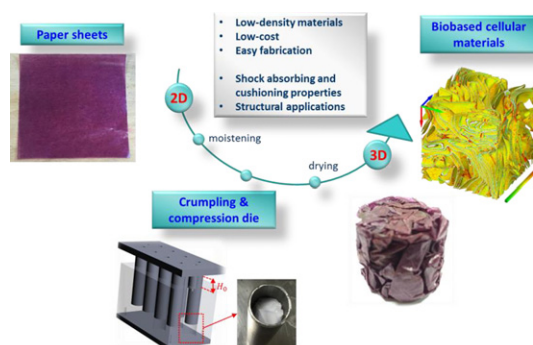
ARTICLE INFO

ABSTRACT

Several low-density crumpled paper-based materials were fabricated by varying both the volume fraction and the geometry and mechanical properties of paper sheets. Their 3D architecture was investigated using X-ray microtomography. Microstructure descriptors such as the pore size distribution, the mean curvature distribution and the volume fraction of ordered domains were finely analyzed. Their mechanical properties were also assessed using uniaxial compression tests. Our results showed that crumpled materials exhibited a particular porous microstructure with a reproducible mechanical behavior between foams and entangled fibrous materials. Their compressive behavior was characterized by successive elastic, strain-hardening and densification regimes. The effects of the geometry, microstructure and mechanical properties of the sheets on the process-induced microstructures and mechanical performances were discussed. In particular, a simple micromechanical approach was used to estimate analytically and from the 3D images the role of ridges and ordered domains on the mechanical properties of crumpled papers. The evolution of their Young's moduli and yield stresses were studied as a function of their relative densities and compared with experimental data available in the literature for other cellular materials, showing that crumpled papers are promising renewable alternatives to standard polymer foams for several engineering applications, due to the proper combination of mechanical properties, porosity, cost, and easy fabrication.

© 2017 Elsevier Ltd. All rights reserved.

---

* Corresponding author at: Univ. Lyon, INSA-Lyon, CNRS UMR 5259, LaMCoS, F-69621 Lyon, France.
E-mail address: florian.martoia@insa-lyon.fr (F. Martoïa).

1. Introduction

Cellular materials are attractive materials for structural applications due to their lightweight and high specific mechanical properties. To date, most studies in the literature have been mainly focused on foams, honeycombs [1,2] and more recently on entangled materials [3,4] or truss microstructures [5]. On the contrary, crumpled materials, and more particularly those prepared from randomly folded thin paper or aluminum sheets, are primarily regarded as model systems by physicists due to their fascinating topology and their related scaling laws close to those observed in many other materials or systems such as for example polymerized membranes, biological cells or plants [6,7]. The use of crumpled sheets as structural materials (e.g. shock absorbers, core of sandwich panels) has been recently introduced by Bouaziz et al. [8] and subsequently taken up by Cottrino et al. [9], Balankin et al. [10] and more recently by Hanaor et al. [11]. In [8–10], dedicated to aluminum foils, the authors showed that crumpled materials could be potentially used in many structural applications due to their high specific mechanical properties, their low-cost and their simple fabrication route. The mechanical properties of crumpled aluminum foils were investigated using both simple compression tests and close die compression experiments. Crumpled aluminum foils exhibited foam-like compression behavior with successive elastic, strain-hardening and densification regimes [8], the second regime being rarely observed with other usual foams and close to that observed for entangled fibrous media [1,12]. In addition, their mechanical properties were also dependent on the initial relative density ρ/ρ_s as other cellular or fibrous materials: both the apparent compression modulus E and yield stress σ_y were power-law functions of ρ/ρ_s [8–10,12]. More recently, Hanaor et al. [11] showed that low-cost and biobased materials such as recycled paper could also be used to fabricate rigid structural materials with varied sizes and geometries. Dense compacted crumpled materials were fabricated by high pressure hydraulic confinement of randomly crumpled tissue papers. The low-cost and biobased materials that were fabricated in their study exhibited high densities ρ in the range 800–1300 kg m^{-3}, and showed high specific mechanical properties (e.g., ultimate compressive strength values of up to 200 MPa) under both quasi-static and high strain rate loading conditions, and deformation energy close to that commonly obtained with many engineering materials of similar density. Hence, these studies have demonstrated that a wide variety of materials with different porosities, geometries and mechanical performances can be potentially fabricated by simply varying the in-plane sizes L of the precursor sheets [8–10], but also by tuning the mechanical behavior of the sheets [13] or even the crumpling process [9,11].

However, the selection and the use of a specific crumpled material for a particular engineering application require a proper control of the process-induced microstructures and a comprehensive understanding of their role on the mechanical behavior [1,13,14]. In the last decade, significant effort was made to understand the physics of crumpling phenomena [15–20] and the microstructures of crumpled sheets [21–26]. Despite this effort, further studies are still required to fully elucidate the links between the three-dimensional self-locked architectures of these cellular materials and their resulting mechanical properties. The crumpling of thin sheets by external forces usually leads to the formation of complex patterns of folds [15,17,22,26]. For example, a remarkable feature of crumpled materials is that their folding microstructure is characterized by the presence of ordered and clustered domains in the form of stacks of layered facets. Lin et al. [25] and Cambou and Menon [23] observed layering phenomena in randomly crumpled aluminum and elastomeric balls. The folding configuration of randomly crushed elastic and elastoplastic sheets was also studied numerically by Tallinen et al. [19]. Their numerical simulations revealed that crumpled elastic sheets were more effectively folded than crumpled elastoplastic sheets. Elastic sheets also exhibited a more layered structure and had a larger characteristic facet size. However, the growth of these ordered domains during the crumpling process, their architecture

and their role on the mechanics of crumpled materials are still poorly understood.

Within this context, this study aimed at (i) exploring whether paper, i.e., a low-cost and widely available biobased material with interesting specific mechanical properties [27], can be used to fabricate low-cost, low-density (i.e., at much lower densities than those investigated in [11]) renewable cellular materials with controlled three-dimensional architectures, (ii) assessing the role of the microstructure features of crumpled papers such as ridges and ordered domains on their mechanical properties, and (iii) exploring their practical interest compared with commercially-available cellular materials such as polymer foams and honeycombs that are widely used for structural applications or even with other emerging biobased porous materials such as, for instance, foams with nanofibrils of cellulose (NFC) prepared by ice templating [28]. Thus, in a first section, we present a simple but efficient fabrication route for obtaining reproducible low-density crumpled paper-based materials. Then, the three-dimensional structure and the mechanical properties of these materials were studied using X-ray microtomography imaging and compression tests, respectively. Several studies [9,22,24] have shown that X-ray tomography is a well-suited tool for characterizing the internal conformation of crumpled sheets. To finely analyze the inner microstructures of crumpled materials and their role on the mechanical properties, we developed and used image analysis procedures to extract several relevant microstructure descriptors such as the pore size and mean curvature distribution, spatial localization and volume fraction of ridges and ordered domains with layers of stacked sheets.

2. Experimental procedure

2.1. Materials and sample preparation

Two types of commercial paper sheets were used, namely a 'tracing' paper and a 'crystal' paper. These papers had a mean thickness of 75 μm and 33 μm, respectively, with practically the same density ρ_p (Table 1). The cross-sectional micrographs shown in the insets of Fig. 1 revealed that both types of paper had quite homogeneous microstructures with a limited amount of flat pores parallel to the sheet mid-plane. These micrographs also showed that both papers exhibited rather rough and irregular surfaces inherited from the papermaking operations.

To characterize the mechanical properties of the paper sheets, uniaxial tensile tests were performed on rectangular specimens (mean width $\approx$ 15 mm and mean initial length $l_0 \approx 100$ mm) at a constant strain-rate $|\dot{\varepsilon}| = 0.01$ s^{-1} using an electromechanical testing machine (Instron 5960, USA) equipped with a force sensor of 5 kN. Before testing, papers were stored for at least 2 days under controlled conditions, i.e., $T = 25$ °C and 50% of relative humidity (RH). To investigate the effect of the fabrication process (described below) on the mechanical properties of initial paper sheets, tensile tests were also performed after the sheets were soaked in water for 60 s and dried in an oven at a temperature of 95 °C. Both types of paper sheets showed an anisotropic elastoplastic behavior characterized by longitudinal (MD) and transverse (CD) Young's moduli E_{MD}, E_{CD}, and yield stresses σ_{yMD}, σ_{yCD}, followed by a strain-hardening regime up to maximal tensile breakage strains (Fig. 1). The tests also showed that the mechanical behavior of initial crystal paper sheets (Fig. 1a,b, red curves) was severely affected by

Table 1
Structural properties of initial paper sheets. Mean values are based on an average of 5 measurements.

	Tracing paper	Crystal paper
Grammage G (g m^{-2})	91 ± 5	41 ± 1
Thickness $\bar{t}$ (μm)	75 ± 2	33 ± 1
Paper density ρ_p (kg m^{-3})	1213 ± 99	1242 ± 68
Porosity $1 - \rho_p/\rho_{cell}$[a]	0.19 ± 0.01	0.17 ± 0.01

[a] $\rho_{cell} = 1500$ kg m^{-3} is the density of the dense cellulose.
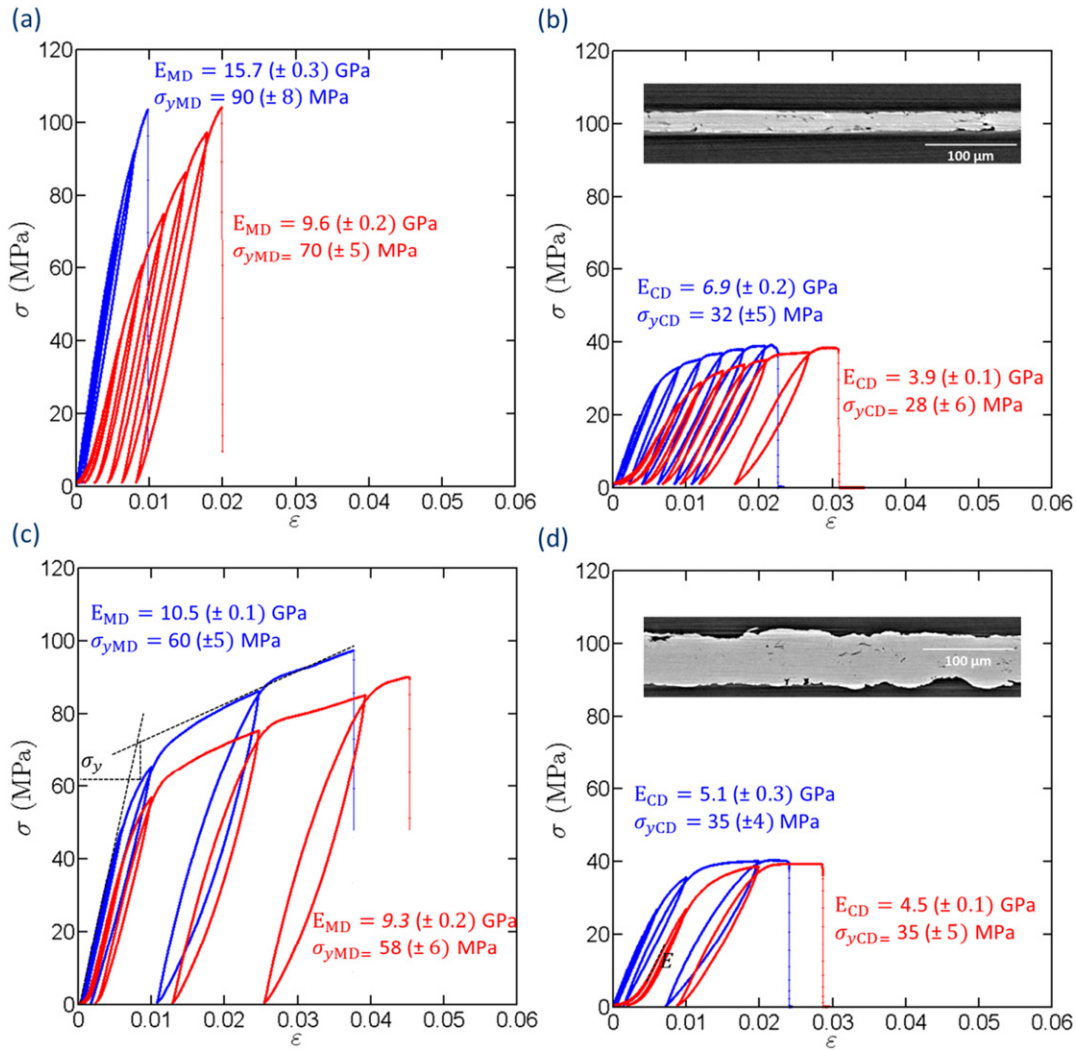
Fig. 1. (a,b) Tensile stress σ as a function of logarithmic (Hencky) strain ε obtained for crystal (a,b) and tracing paper sheets (c,d) in the machine direction (MD) (a,c) and in the cross direction (CD) (b, d). The blue curves correspond to the mechanical response of initial sheets, whereas the red curves correspond to the mechanical behavior of paper sheets after being soaked in water for 60 s and dried in an oven at a temperature of 95 °C. The insets of figures b,d correspond to 2D cross section views of (b) crystal and (d) tracing paper obtained using X-ray synchrotron microtomography (voxel size: 0.6^3 μm³). The Young's moduli and yield stresses reported in these graphs are based on an average of 5 measurements. The first were estimated at the onset of unloading specimen after stretching them up to $\varepsilon \approx 0.005$, the second were estimated according to the method shown in (c).

moistening and drying operations (Fig. 1a,b, blue curves), whereas that of tracing paper sheets remained practically unchanged (Fig. 1c,d, blue curves). After moistening and drying, it is interesting to note that both types of paper sheets exhibited similar mean Young's moduli $\bar{E}_p = (E_{MD} + E_{CD})/2 \approx 7$ GPa and mean yield stresses $\overline{\sigma}_{yp} = (\sigma_{MD} + \sigma_{CD})/2 \approx 48$ MPa. Hence, the two types of papers chosen in this study (with similar mechanical properties after crumpling) allowed the effect of the sheet thickness and geometry on the process-induced microstructures of crumpled materials to be properly investigated.

Crumpled paper-based materials were obtained using the fabrication route shown in Fig. 2. Each paper sheet was soaked in a water bath for 60 s and then drained to remove the excess of water at their surface. The sheets had a relative water content of about 40 wt% after this step. Then, moistened sheets were 'randomly' crumpled by hand into the form of a ball (Fig. 2) and inserted into a cylindrical die to obtain cylindrical samples (initial diameter $D_0 = 30$ mm and height $H_0 = 30$ mm). Then, the mold was placed into an oven at a temperature of 95 °C for 24 h. Finally, the resulting cylindrical crumpled structures (Fig. 2) were removed from the mold and stored in controlled conditions ($T = 45$ °C, relative humidity of 50%) for at least two days. To

prepare crumpled structures with various initial relative densities ρ/ρ_p, where ρ is the density of the crumpled material before compression, squared sheets with different initial sizes L were used (Table 2).

Lastly, to study the effects of the sheet type, several crumpled materials were also fabricated using randomly folded aluminum foils that had a prominent plastic behavior (ductile elastoplastic behavior, elastic modulus $\bar{E}_p = 40$ GPa, yield stress $\overline{\sigma}_{yp} = 52$ MPa). For that purpose, commercial aluminum foils of different sizes (density $\rho_p = 2500$ kg m⁻³, thickness $\bar{t} = 43$ μm) were hand-crumpled and compressed into the cylindrical die shown in Fig. 2, i.e., using the same mechanical route used to prepare paper samples.

2.2. X-ray microtomography

The 3D architecture of crumpled tracing papers was characterized using a laboratory X-ray microtomograph (3SR Lab, RX Solutions, France). A voxel size of 15^3 μm³ was chosen to obtain 3D images. The samples were fixed onto a rotation stage between the conical X-ray source and the detection unit that recorded the transmitted X-rays.
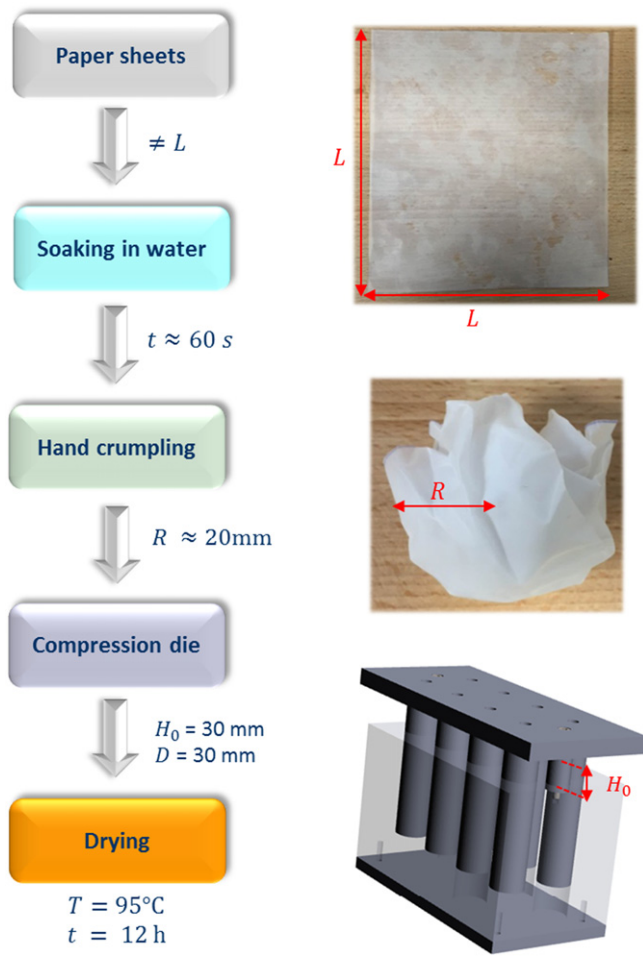
Fig. 2. Scheme of the procedure used to fabricate crumpled paper-based materials. The fabricated samples were conditioned in controlled environmental conditions ($T = 25$ °C, relative humidity of 50%) for at least two days before testing.

Samples were rotated under the beam incrementally up to 180° to provide a set of 1500 radiographs (duration of the scan $\approx$ 1 h). The 3D microstructure of crumpled crystal sheets were characterized using a high-resolution X-ray synchrotron microtomograph (ID 19 beamline, ESRF, France). This beamline delivers an intense coherent and monochromatic X-ray source and enables images with a high signal-to-noise ratio to be acquired. The X-ray energy and the number of radiographs were set to 19 keV and 3000, respectively (duration of scan $\approx$ 60 s). A voxel size of 5.5^3 μm³ was chosen to obtain accurate representation of the imaged crumpled sheets. Then, 3D images were reconstructed using the so-called Paganin procedure, which is based on the

Table 2
Lengths L of the initial paper sheets used to fabricate crumpled samples. The density ρ and the relative density ρ/ρ_p of the resulting crumpled materials are also reported (note that the sample porosity is equal to $1 - \rho/\rho_p$).

Sample	Initial length L (mm)	Initial density ρ (kg m^{-3})	Initial relative density ρ/ρ_p
Tracing paper	140	85	0.07
	170	121	0.1
	205	182	0.15
	235	243	0.2
	290	340	0.28
	315	412	0.34
Crystal paper	140	35	0.028
	195	68	0.055
	230	109	0.088
	300	211	0.17

use of the phase contrast in the images [29,30]. The two voxels sizes of 15^3 μm³ and 5.5^3 μm³ were chosen to ensure a minimum and identical number of 5–6 voxels in the thickness of both tracing and crystal paper sheets, respectively. This was chosen purposely to minimize errors during the computation of microstructure descriptors (e.g. the mean curvature), to get similar systematic errors during the subsequent image analysis subroutines (see below), and to allow a relevant analysis and comparison of the two types of crumpled sheets.

2.3. Image analysis

Due to the good contrast between the papers and the pores, the 3D images could be segmented without difficulty in order to separate the porous and the solid phases of the crumpled materials. This was done using an automatic threshold (based on the Otsu's method [31]) implemented in the freeware ImageJ [32]. Then, the homogeneity of the samples was assessed using profiles of their relative density along their height and radius [3,8]. The degree of anisotropy (tDA) was determined using the mean intercept length (MIL) method [33] implemented in the plugin BoneJ of ImageJ [34]. The fractal dimension of the crumpled materials was also calculated from the binarized stacks using a box-counting method implemented in BoneJ [34,35]. Crumpled materials exhibit particular three-dimensional architectures in which the porosity is almost entirely connected [8,9]. Consequently, measuring a typical pore size and anisotropy in these interconnected and continuous systems is not a trivial procedure. In this study, these measurements were achieved by applying sequential 3D morphological erosion and dilatation operations of increasing size to the porous phase. Hence, the size measured using this computational processing procedure corresponds to the Euclidian thickness of the porosity [36]. The volumetric pore size distribution of paper-based crumpled materials was determined using the 3D granulometry function provided by the plugin Analysis 3D (ImageJ) [37]. This measurement was performed using octahedron structural elements.

To locate and assess the volume fraction of ordered domains in the crumpled structures, i.e., with layers of stacked facets [19,23,25], a dedicated procedure was developed, as sketched in Fig. 3. The 3D binarized images were dilated several times (3, 5, 8 and 10 times for crumpled tracing sheets and 3, 7, 10 and 13 times for crumpled crystal sheets) using the DilEro function provided by the plugin Analysis 3D [37] and then reversely eroded (steps 1 and 2 in Fig. 3) to fill the gap between neighboring sheets. Then, the local thickness was computed at each point in the solid phase of the resulting images using the thickness function provided by the plugin BoneJ to obtain 3D thickness maps (step 3). A thresholding of the false-color thickness map was applied to keep only the zones in the crumpled structure with the highest thicknesses which corresponded to the stacks of layered sheets (step 4). Finally, the as-obtained images were compared to the original images to keep only the set of voxels that overlapped (step 5). This was performed using the image calculator function implemented in ImageJ [32]. Hence, this procedure enabled the volume fraction of ordered domains ϕ_c and the volume fraction of paper ϕ_{cp} in these domains to be determined. More particularly, ϕ_c was determined by counting the number of voxels of the paper phase (step 5) and dividing it by the total number of voxels of the region of interest (ROI). The volume fraction of paper in ordered domains ϕ_{cp} was determined by counting the number of voxels of the paper phase of the ordered domains (step 5) and dividing it by the total number of voxels of the zones in the crumpled structures with the highest thicknesses (step 4).

Curvature maps and distributions were also computed from the tomographic images. For that purpose, the mean curvature $\mathscr{H}$, defined as half the sum of the two principal curvatures κ_1 and κ_2, i.e., $\mathscr{H} = (\kappa_1 + \kappa_2)/2$, was obtained in each point of the paper-pore interface. Many techniques are available to estimate the local mean curvatures from either triangular or digital surfaces [38–41]. These estimators often imply some accuracy issues since they are inherently second-order local
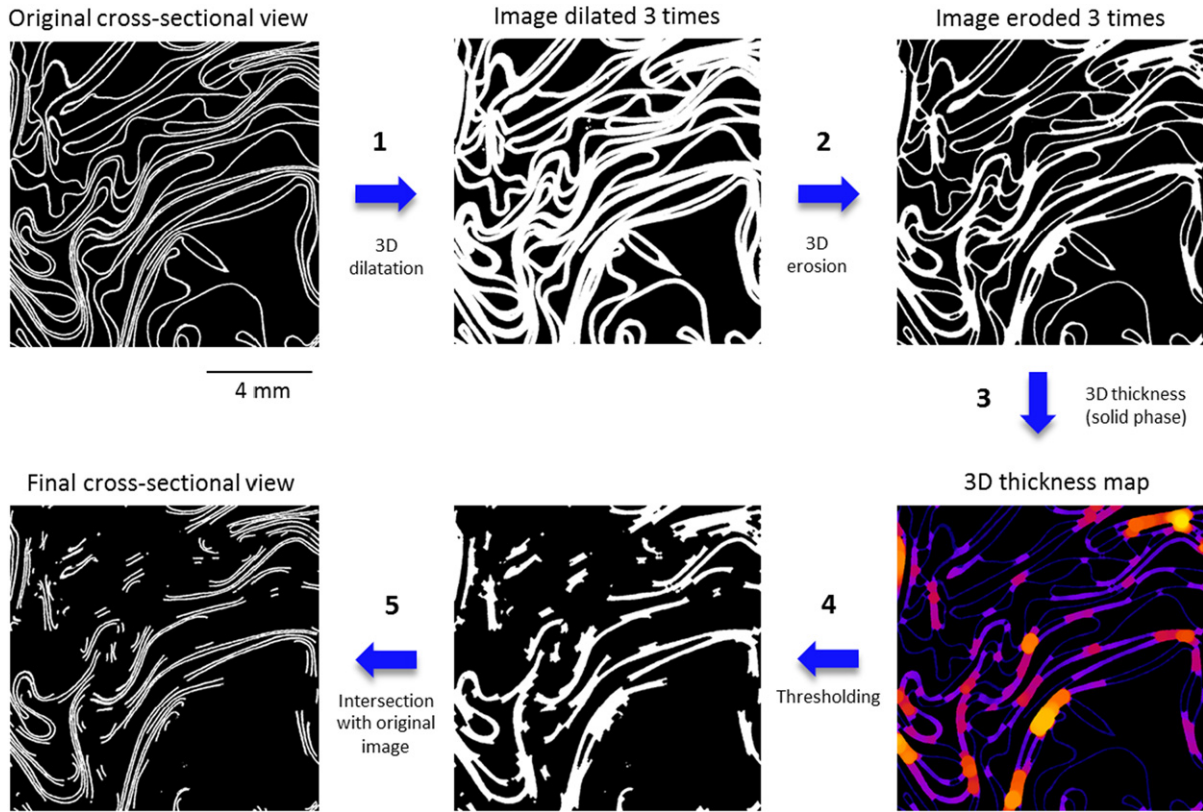
Original cross-sectional view Image dilated 3 times Image eroded 3 times

1

3D
dilatation

2

3D
erosion

4 mm

3

3D thickness
(solid phase)

Final cross-sectional view 3D thickness map

5

Intersection
with original
image

4

Thresholding

Fig. 3. Set of image processing operations applied on binarized stacks to separate the layered domains in crumpled materials.

derivatives, which are sensitive to noise and digitization effects. In the present approach, the mean curvatures were adaptively computed from the largest 'relevant' neighborhoods, limiting the digitization noise (see [42] for more details). Briefly, the method is based on the following expression of $\mathcal{H}$ [43], where the mean curvature at an interface point P between the papers and the pores is defined as the divergence of the outward unit normal vector $\boldsymbol{n}(P)$:

$$\mathcal{H}(P) = \frac{\nabla \cdot \boldsymbol{n}(P)}{2} \qquad (1)$$

To estimate $\boldsymbol{n}(P)$, we relied on an adaptive method which used the volumetric information of the signed distance map to infer both $\boldsymbol{n}(P)$ and its most relevant neighborhood, depending on the local morphology of the interface [44]. The distributions of $|\mathcal{H}|$, expressed in terms of occurrence ratio per curvature range, were then computed: they provided the ratio in percentage of the paper's surface area that was located within a particular range of $|\mathcal{H}|$. To rule out some potential side effects due to the border of the image proximity, we suppressed from the statistics all curvatures $\mathcal{H}(P)$ values whose P-to-border-distance was lower than a maximal radius (here, 5 voxels) of the curvature estimation neighborhood.

2.4. Uniaxial compression tests

Uniaxial compression experiments were performed on cylindrical specimens in controlled environmental conditions ($T = 25\ °C$ and 50% RH). To investigate the effect of the relative humidity on the mechanical properties of crumpled paper-based materials, some tests were also performed at 20% and 85% RH. For that purpose, a chamber connected to an air humidity generator (TECHPAP, France), surrounding both the compression plates and the specimens, was installed in the compression machine. Crumpled materials were subjected to five successive load-unload cycles and at a constant compression strain-rate of $|\dot{\varepsilon}| =$

0.002 s^{-1} with increasing the global axial compression Hencky strain $\varepsilon_h = \ln(H/H_0)$ upon loading, H being the current height of the sample. These experiments were performed using an electromechanical testing machine (DY26, MTS, USA) equipped with a force sensor of either 500 N or 20 kN, depending on the initial relative density ρ/ρ_p of the studied materials. During the experiments, the nominal compression stress $\sigma = 4F/\pi D_0^2$ was also acquired (F being the compression force). The evolution of the geometry of the samples was observed using images taken during the tests with a CCD camera (Jai Pulnix RM-4200GE, spatial resolution 2048×2048 pixels). It was also checked that the stiffness of the entire testing device was much higher than those of crumpled materials, so that ε_H was considered to be a relevant macroscale axial deformation of samples. The compression moduli E of the samples were calculated at the onset of the second unloading stage ($\varepsilon_H \approx 0.1$) [8]. The apparent yield stress σ_y was determined from the intersection of the two tangent lines parallel to the elastic domain and the nearly linear strain hardening plasticity regime above the yield stress [1,28] (see Fig. 9a).

3. Results

3.1. Microstructure of crumpled paper sheets

Fig. 4 shows the internal microstructure of several crumpled materials obtained using tracing and crystal paper sheets at various packing fractions that ranged from 0.07 to 0.36. The colormaps plotted onto the sample surfaces are related to the local mean curvatures. The figure shows that the initial sheets were severely bent and distorted during sample processing to form complex self-locked architectures, *i.e.*, with many ridges or vertices (red and green surface zones of the 3D images, respectively) and curved thin walls (yellow surface zones). The fractal dimension of the samples increased from approximatively 2.4 for the lowest initial relative density up to 2.8 for the highest initial relative density, showing a progressive change from a 2D material (uncrumpled
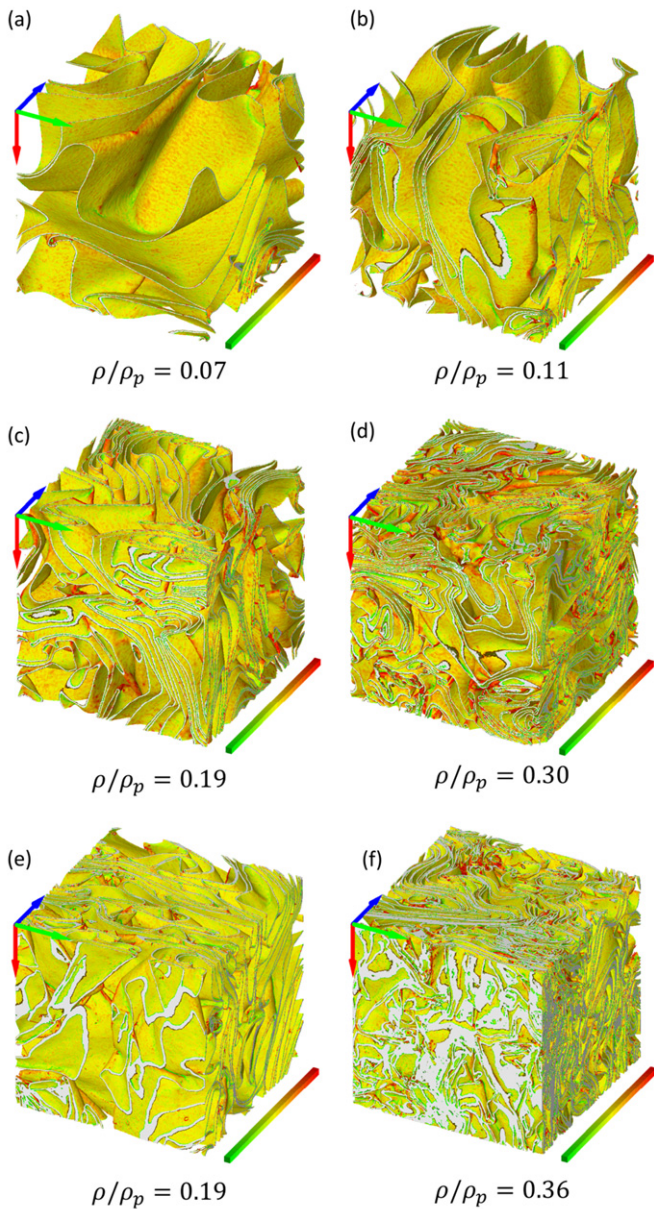
Fig. 4. 3D views of crumpled tracing sheets (a–d) and crystal sheets (e–f). The colormaps represent the mean curvature of the sheets (see Section 2.3) that range from -50 mm^{-1} (green, concave shape) to 50 mm^{-1} (red, convex shape). For better visualization, curvatures are represented on all interface points, excepting at the intersection with image borders, where bulk paper is represented in light gray. Images (a–d) and (e,f) have a size of $12 \times 12 \times 12$ mm^3 and $6.6 \times 6.6 \times 6.6$ mm^3, respectively. The arrows in blue, green and red correspond to the x, y and z directions of the images, respectively. Note that the relative densities ρ/ρ_p displayed in this figure were calculated by counting the number of voxels of the paper phase and dividing it by the total number of voxels of the ROIs.

sheet where the fractal dimension is close to 2) to a 3D compact structure as the relative density ρ/ρ_p was increased. These values are in accordance with those reported by Lin et al. [24] for randomly crumpled aluminum balls. Indeed, the authors also observed an increase in the fractal dimension (from 2.3 to 2.8) with increasing isostatic compaction.

In addition, regardless of the imaged samples, the mean degree of anisotropy (tDA) was close to 2.5. This value corresponds to rather isotropic initial structure (tDA tends to infinity for a fully aligned structure [34]). Besides, a finer analysis of the stack of binarized images shown in

Fig. 5 revealed that the local relative density of the samples was nearly constant along the height of the samples. The local relative density estimated along the radius was also nearly constant over a wide distance from the center of the samples. Similar local density profiles, characterized by a drop of the local sheet volume fraction near the free surfaces of the samples were also reported previously for crumpled aluminum foils [8,9] but also for compacted entangled monofilaments [3]. The routes used to manufacture these materials as well as their particular architectures induced these edges effects. Indeed, near their free surfaces, the entanglement is possibly lower, leading to higher elastic sheet recovery after crumpling and compacting the samples, and thus to lower relative densities in these regions.

3.1.1. Pore size distribution

The pore size distribution within the imaged samples is shown in Fig. 6a,b. As expected, the typical pore sizes decreased significantly with increasing the sheet packing fraction and were smaller for crystal paper. The characteristic pore size $\bar{d}$ which corresponds to the pore size of the highest peak in the distribution decreased from 1770 μm to 180 μm for tracing sheets and from 190 μm to 44 μm for crystal sheets, as the initial relative density ρ/ρ_p increased from 0.07 to 0.3 and from 0.19 to 0.36, respectively. The pore size range also extended to smaller values with increasing the sheet packing fraction, suggesting that the pores that were formed during compaction of the sheet were less polydisperse.

However, it is interesting to note that the dimensionless pore size $\bar{d}/\bar{t}$ at $\rho/\rho_p = 0.19$ was very similar for both types of paper. In addition, Fig. 6c also shows that the ratio $\bar{t}/\bar{d}$ was a power-law function of ρ/ρ_p, i.e., $\bar{t}/\bar{d} \propto (\rho/\rho_p)^a$, with $a = 1.7$, regardless of the considered paper. These two points suggest that the morphology of the pores was nearly similar for both types of materials.

3.1.2. Ordered domains

As already emphasized in several studies [19,23,25], the 3D images shown in Fig. 4 reveals the coexistence of disordered crumpled zones with zones that exhibit stacked layers of sheets with higher local relative density (see also Fig. 3). Stacked layers induced during the sample fabrication were homogeneously distributed in samples and displayed 3D random orientation (Fig. 5). Both the volume fraction of ordered stacks and the number of layers in each stack increased with the relative density. From the segmented 3D rendered perspectives views shown in Fig. 7, it is seen that the thicknesses between the parallel flat facets in the stacks progressively decreased and that the volume fraction of sheets in close contact increased with the compaction of the crumpled sheets. A quantitative analysis of the segmented 3D images is presented in Fig. 7a,b,c. From these graphs, several remarks can be drawn:

- Fig. 7b shows that the volume fraction of layered domains ϕ_c was a power-law function of the sample relative density, i.e., $\phi_c \propto (\rho/\rho_p)^b$, with $b = 1.5$. These ordered domains were formed even at low relative density, i.e., $\rho/\rho_p = 0.07$ and represented up to 95% of the sheet volume for the highest crumpled densities ($\rho/\rho_p = 0.3$) (Fig. 7a).
- In addition, Fig. 7c shows that the volume fraction of paper ϕ_{cp} in the ordered domains was close to 0.5. This value is considerably higher than the relative bulk density ρ/ρ_p of crumpled samples. It is also interesting to note that ϕ_{cp} remained nearly constant whatever the considered crumpled sample: this is presumably link to the existence of a limiting value of curvature radius which prevents the paper sheets to be folded into more densely packed domains (this point will be further discussed in the next subsection and in Section 4.1).
- Finally, Fig. 7a reveals that for a given relative density of $\rho/\rho_p = 0.2$, both types of crumpled materials, i.e., made either with crystal or tracing papers, exhibited these layering phenomena with similar fractions of ordered domains. This suggests that for similar mechanical properties of the parent sheets, the fraction of ordered domains does not
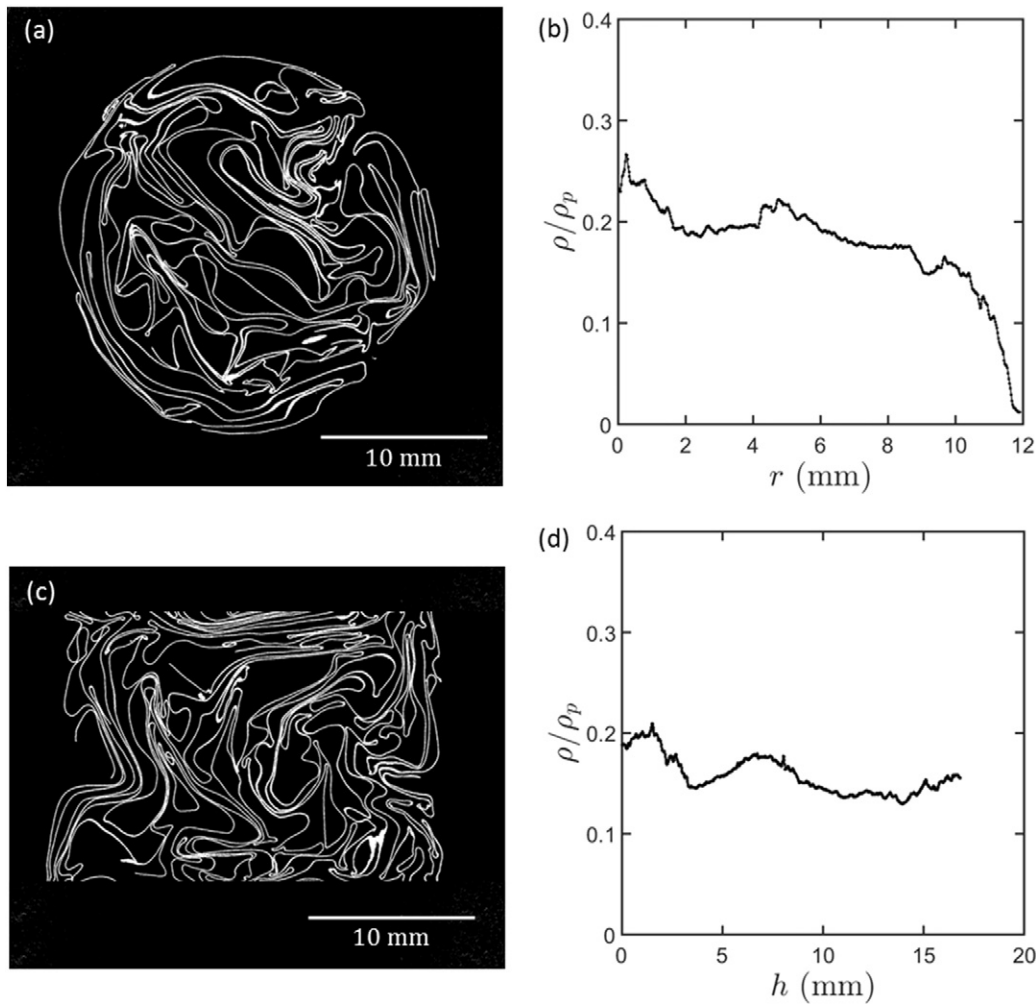
Fig. 5. Radial (a) and vertical (b) cross sections of a randomly crumpled tracing paper (initial height of $H_0 = 20$ mm and diameter of $D_0 = 25$ mm) with a macroscale relative density of $\rho/\rho_p = 0.17$. Graphs (b,d) show the local relative density ρ/ρ_p along the radius (b) or height (d) of the sample.

depend significantly on the geometry and structural characteristics of the parent sheets but mainly on the sheet packing fraction.

3.1.3. Sheet curvature

A remarkable feature of the three-dimensional arrangements of crumpled materials was that a large fraction of the surface area of the sheets was relatively flat (see the yellow regions in the tomographic images shown in Fig. 4). The curvature imposed on the paper sheet by external confinement was concentrated mostly in a network of ridges which met at vertices and corners. In these regions, the strains induced during crumpling exceeded the yield strain of the sheet and the ridges became irreversibly creased into folds. As for the other structure descriptors, Fig. 8a shows that at given paper content, tracing and crystal crumpled sheets displayed practically the same distribution of dimensionless mean curvature $\mathscr{H}\bar{t}$, suggesting again that the morphology of the pattern of folds formed during crumpling was comparable. In addition, Fig. 8b reveals that the fraction of the surface area of the sheet with large curvatures progressively increased with increasing the sheet packing fraction ρ/ρ_p. To analyze more deeply these histograms, regions of high curvatures such as ridges and vertices were identified by considering that they had curvature radius lower than $4\bar{t}$ (Fig. 8b). This threshold value was reasonably chosen by analyzing finely the 3D images (see the image insets of Fig. 8c–d). Fig. 8c shows that the volume fraction of the regions of high curvatures ϕ_r was a power-law function of the sample

relative density ρ/ρ_p, i.e., $\phi_r \propto (\rho/\rho_p)^c$, with $c = 1.7$, whereas their mean dimensionless curvature radius $\bar{R}/\bar{t}$ tended to a constant value close to 1.8 (Fig. 8d). In the same time, it is worth noting that outside these zones, $\bar{R}/\bar{t}$ exhibited a constant decrease, as shown in Fig. 8e.

3.2. Mechanical properties

3.2.1. Typical compression behavior

Fig. 9 shows a collection of macroscale compression stress-strain curves obtained for both types of crumpled materials. These compression curves are typical of many elastoplastic cellular materials and exhibit three distinct regimes:

- An initial quasi-linear behavior up to an initial yield stress σ_y.
- Above σ_y, a marked plastic deformation with pronounced residual strain upon unloading. In this regime, the consolidation of the materials occurs, and the stress σ is an increasing function of the compression strain ε_H. The strain hardening regime is different from the horizontal plateau commonly observed during the consolidation of most elastoplastic foams or even during buckling of honeycomb structures. Here, the strain hardening behavior is potentially controlled by the rearrangement of the crumpling network accompanied by the formation of new ridges and folds with increasing ε_H.
- At high compression strains, a densification regime characterized by a sharp increase in the compressive stress σ.

(a)

(b)

(c)

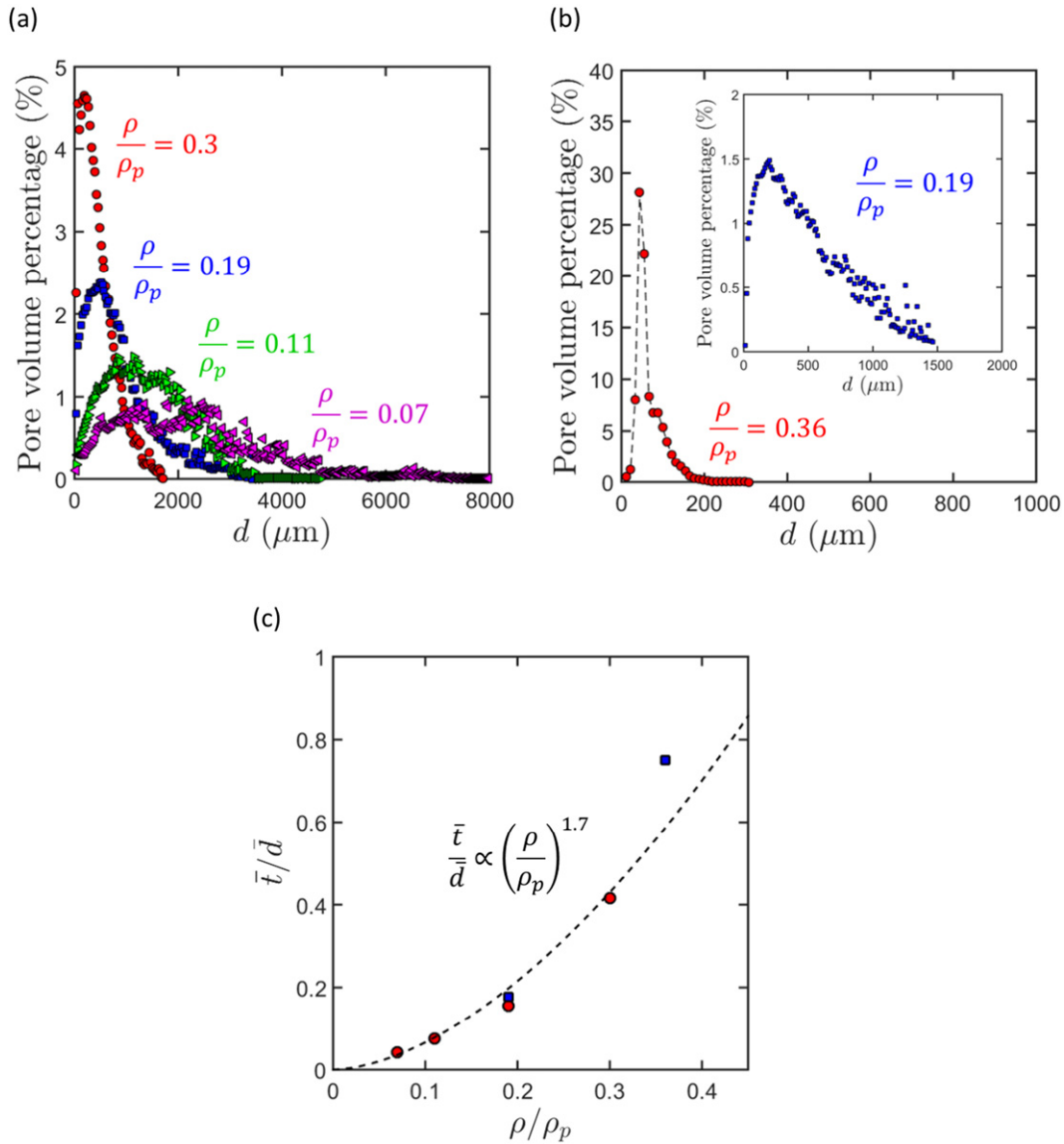$$\frac{\bar{t}}{\bar{d}} \propto \left(\frac{\rho}{\rho_p}\right)^{1.7}$$

Fig. 6. Volumetric pore size distribution obtained for crumpled tracing (a) and crystal (b) papers for different initial relative densities. (c) Graph that shows the evolution of $\bar{t}/\bar{d}$, i.e., the ratio of the sheet thickness $\bar{t}$ over the mean pore size $\bar{d}$, as a function of the initial relative density ρ/ρ_p.

Fig. 9 also reveals that both types of materials exhibited a pronounced non-linear strain recovery upon unloading stages. This suggests that the elastic energy stored within the network of ridges, corners and plates upon loading was sufficient to unfold them partially upon unloading. The recovered strain after the last unloading stage (Fig. 9) was followed by time-dependent (delayed) free-stress strain recovery: after two weeks, the initial residual strain of $\varepsilon_H \approx 0.7$ recorded at the end of the tests plotted in Fig. 9 reduced up to $\varepsilon_H \approx 0.3$. This remarkable feature is different from that observed in crumpled aluminum structures [8] where the elastic recovery is limited, permanent and associated with the irreversible plastic deformation of the aluminum foils. For paper materials, the origin of this recovery is presumably associated to their viscoelasticity [27]. Lastly, the image insets in Fig. 9b show that below a macroscale compression Hencky strain of $\varepsilon_H = 0.2$, the sample deformation was practically homogeneous and exhibited weak transverse deformation (tangent Poisson's ratio $\nu \approx 0$). Above this value, small bulging effects was noticed and was mainly due to frictions of samples with the compression platens and probably due to an increase of the tangent Poisson's ratio.

Furthermore, it is interesting to notice that the tested crumpled paper-based specimens exhibited a reproducible compression behavior at sufficiently high relative densities ($\rho/\rho_p \geq 0.15$ and $\rho/\rho_p \geq 0.055$ for tracing and crystal papers, respectively), i.e., with small stress variation $\Delta\sigma \approx \pm 10 - 20\%$. However, $\Delta\sigma$ increased at lower relative densities. In this low packing regime, the mechanical response was affected by the size and the heterogeneity of the pattern of folds formed during crumpling. As mentioned earlier, the characteristic size of the network of ridges increased with decreasing L in a given volume.

3.2.2. Effect of the initial relative density and relative humidity

Fig. 10a,b shows the evolution of the elastic modulus E and the yield stress σ_y as a function of the initial relative density ρ/ρ_p for tracing and crystal crumpled sheets, respectively. These graphs reveal that E and σ_y were both power-law functions of ρ/ρ_p, i.e., $E \propto (\rho/\rho_p)^n$ and $\sigma_y \propto (\rho/\rho_p)^m$, with $n = 1.7$ and $m = 2$. Both types of crumpled structures, i.e., made either with tracing or crystal papers, exhibited identical scaling exponents and mechanical performances.
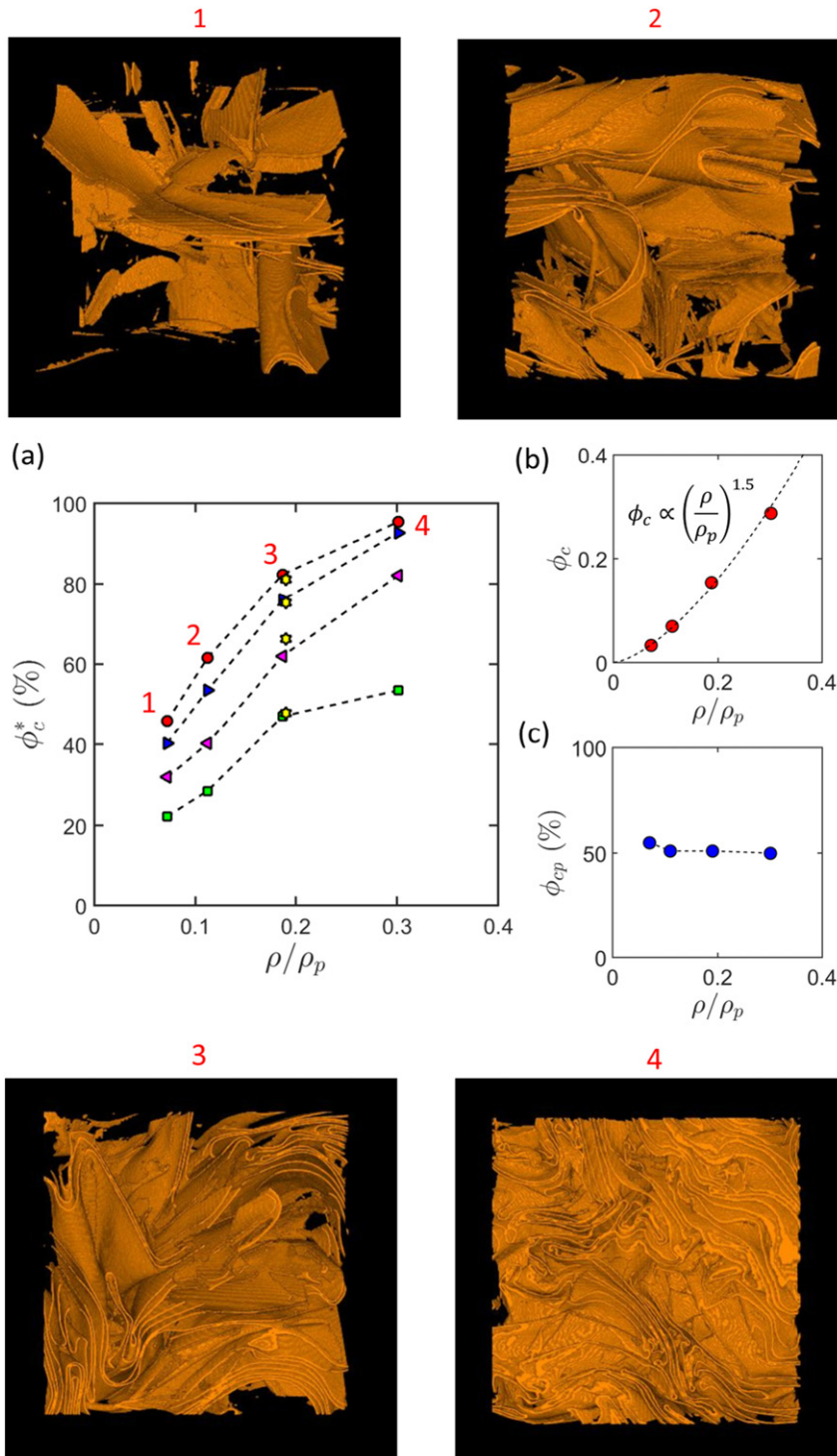
Fig. 7. (a) Evolution of the relative volume fraction of layered stacks $\phi^*_c = \phi_c/(\rho/\rho_p)$ as a function of the relative density ρ/ρ_p. The green, magenta, blue and red symbols were obtained for the tracing paper. They correspond to values of ϕ_c obtained by keeping only the ordered zones with a thickness t_c between the interlayered sheets of interlayer thickness equal to $\bar{t}$, $2\bar{t}$, $3\bar{t}$ and $4\bar{t}$, respectively. The yellow star symbols were estimated with a crumpled crystal sheet. The 3D views (size of $12 \times 12 \times 12$ mm^3) represent the layered domains in crumpled tracing materials for different relative densities and for an interlayer thickness of $4\bar{t}$. (b) Volume fraction of ordered zones ϕ_c (obtained for $t_c = 4\bar{t}$) as a function of ρ/ρ_p. (c) Evolution of the volume fraction of paper ϕ_{cp} in ordered domains.

The mechanical properties of crumpled crystal materials decreased with increasing the relative humidity, as shown in Fig. 10c,d. Indeed, the compression modulus E and the yield stress σ_y decreased by a factor of 2 and 3 with increasing the relative humidity from 20% to 80%, respectively. Papers are fibrous materials made up of cellulose fibers which are hydrophilic, thus they display moisture dependent physical and mechanical properties [27]. However, it is interesting to notice

that the scaling exponents n and m obtained for E and σ_y remained unchanged under different relative humidities. This suggests that the structural and mechanical properties of the initial paper sheets have a minor effect on the mechanics, namely the deformation micro-mechanisms of the ridges and plates which occur when crumpled paper-based structures are subjected to external loadings (this point is further discussed in Section 4).
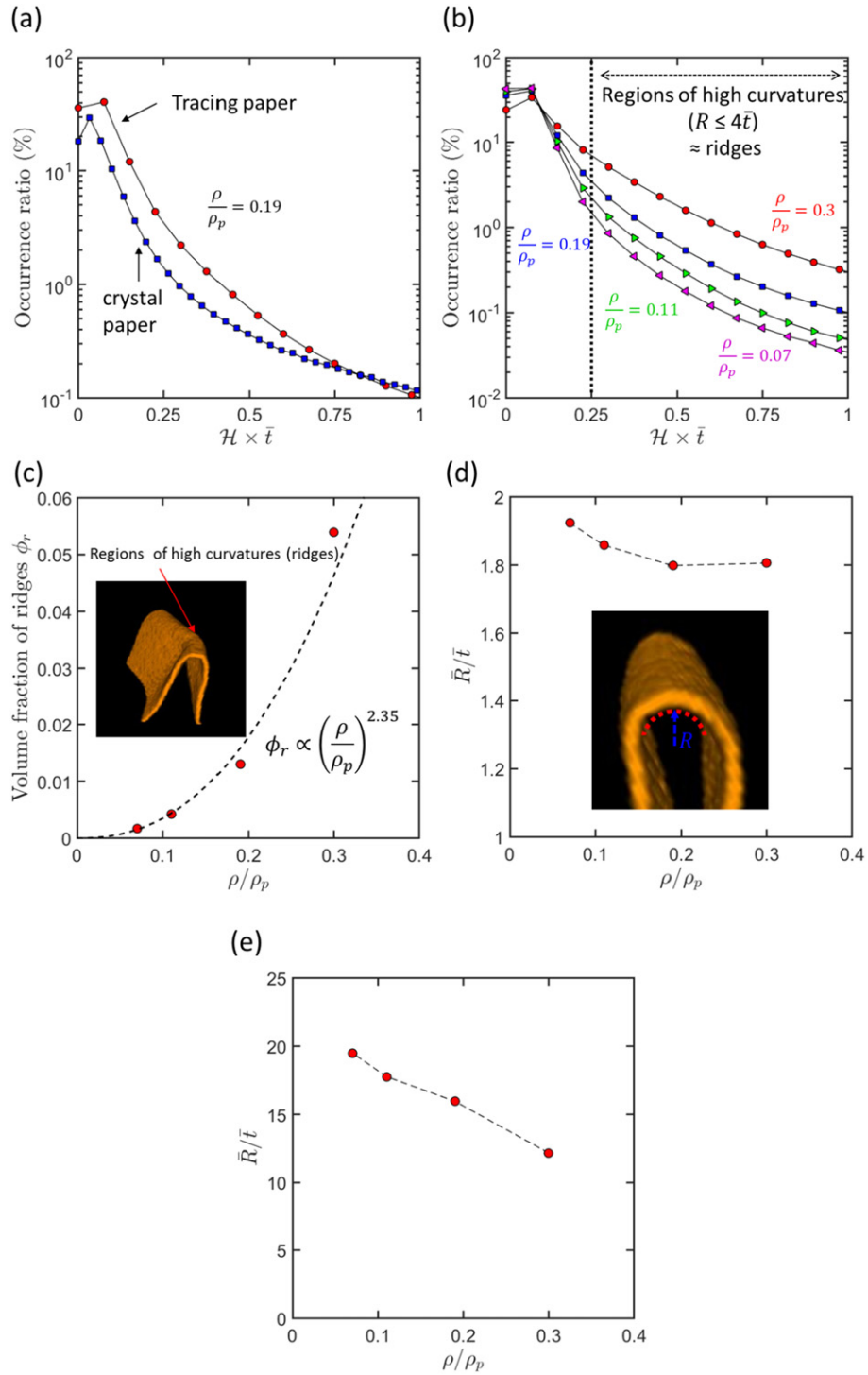
Fig. 8. Distribution of the dimensionless mean curvature $\mathcal{H} \times \bar{t}$ for two crumpled samples with identical relative density ρ/ρ_p of 0.19 and made either with tracing (blue square symbols) and crystal (red circle symbols) paper sheets (a). Distribution of the dimensionless mean curvature $\mathcal{H} \times \bar{t}$ of crumpled tracing samples shown in Fig. 3a–d (b). Volume fraction of the sheet with a dimensionless mean curvature $\mathcal{H} \times \bar{t} > 0.25$ (i.e., $\bar{R} < 4\bar{t}$), namely the ridges, as a function of the initial relative density of crumpled tracing samples (c). Dimensionless mean curvature radius for the fraction of surface area of the sheet with $\mathcal{H} \times \bar{t} > 0.25$ (ridges) (d) or $\mathcal{H} \times \bar{t} < 0.25$ (e) as a function of the initial relative density.

4. Discussion

The experimental results presented in the previous section clearly showed that the mechanical properties of the sheets as well as the process-induced microstructures had noticeable effects on the mechanical properties of crumpled sheets. These effects are further discussed in the following subsections.

4.1. Crumpling mechanisms and related microstructures

The sheet packing fraction ρ/ρ_p affects significantly the characteristic pore size $\bar{d}$ of crumpling networks (Fig. 6). More particularly, Fig. 6 shows that $\bar{d}$ is a power-law function of $(\rho/\rho_p)^{-a}$, with $a = 1.7$. This power-law exponent is different from that theoretically expected for the characteristic dimensions of inter-fiber voids in isotropic networks
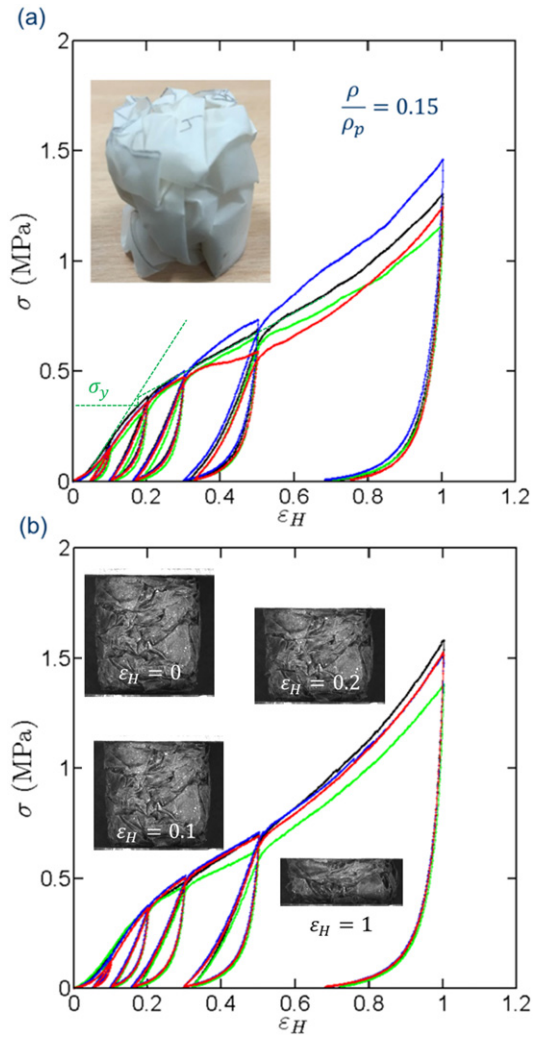
Fig. 9. Stress-strain curves of crumpled structures obtained during the compression of tracing (a) and crystal (b) paper sheets with very close relative density. The image insets show the evolution of the geometry of a crumpled crystal sample during simple compression.

of entangled fibers ($a = 0.5$) [45,46]. This exponent is also quite different from that expected for classical cellular materials with regular architectures such as closed ($a = 1$) and open foams ($a = 0.5$) [1]. Thus, crumpled materials constitute a new class of porous materials with structural and thus mechanical features (see below) different from standard foams and fibrous materials.

These features are inherited from the crumpling process. During compaction, paper sheets were increasingly bent and the existing folds were presumably compressed to sharper dihedral angles. The deformation of the sheets was also presumably associated with the formation of new crumpling ridges. Indeed, it has been reported by Cambou and Menon [22], that there is a limiting value of curvature beyond which the crumpling process leads to the formation of new ridges rather than deforming existing folds. Results obtained in this work are in agreement with this mechanism. As reported in Fig. 8d, a limiting value of the dimensionless curvature radius is observed close to 1.8 and occurred at relatively low relative densities (between 0.1 and 0.2). This suggests that the sharp increase of the volume fraction shown in Fig. 8c could be mainly related to the creation of new folds. Fig. 7 also proved that this creation of new folds was mainly correlated to the formation of clustered and ordered domains, at least for the low relative density regime. These domains probably correspond to proper topological configurations that minimized the deformation energy of those systems during crumpling. This mechanism

leads to large ordered domains with low mean curvature (see the tomographic images 1 and 2 in Fig. 7). However, at higher relative densities, the growth of these domains is progressively restrained with increasing the relative densities (Fig. 7). In this situation, the crumpling process leads to the bending/folding (see the two tomographic images 3 and 4 below the graph of Fig. 7 and the graph of Fig. 8e) and the consolidation of ordered domains.

4.2. Links between microstructure and mechanics of crumpled materials

4.2.1. Scaling laws

The scaling exponents ($n = 1.7$ and $m = 2$) obtained for the mechanical properties of crumpled paper-based materials were close to those commonly expected for classical cellular materials with well-controlled microstructures and deformation mechanisms, such as open ($n = 2$, and $m = 1.5$) or closed foams with thickening of cell edges ($1 < n < 2$ and $1 < m < 1.5$) [1]. More particularly, these exponents suggest that the compression behavior of crumpled paper-based materials could result from multiple combined deformation micro-mechanisms such as bending of the ridges associated to bending and stretching/compression of the multiple interlocked thin plates [1,8,10]. The initial deformation of crumpled paper-based samples is potentially associated with changes of radius of curvature, accompanied with the bending and stretching/compression of the ridges (seen as struts). The interlocked thin plates (that can be seen as thin cell walls) could also bend under deformation. Once the compression stress exceeds the yield stress σ_y, the deformation of crumpled samples is presumably controlled by the buckling/bending of ridges and formation of new crumpling ridges, as well as the rearrangement of crumpling network. The numerous ordered domains that are homogeneously and isotropically distributed in the bulk of the materials (Figs. 4 and 5) could also contribute to the mechanical strength. On the one hand, ordered domains with numerous layers of stacked sheets could be seen as plates with high thicknesses and thus high stiffness that could potentially strengthen crumpled materials, as suggested in previous studies [22,23]. On the other hand, as the creation of these domains could be associated to the minimization of the deformation energy during crumpling (see previous subsection), one could also expect that they contribute to the minimization of the mechanical properties of manufactured crumpled samples.

The link between the microstructure and the mechanical properties of crumpled materials is still not well established owing to the variety and complexity of deformation mechanisms occurring in the different parts of the crumpled sheet, namely the ridges (r) and the facets stacked in the clustered/ordered domains (c) or out (e) of these domains. However, using simplified micromechanical assumptions, a possible scenario can be proposed to identify the elementary mechanisms that mainly contribute to the elastic deformation of crumpled samples. Indeed, in the elastic regime, the strain energy $\mathcal{E}$ (per unit of volume of crumpled paper) of a loaded crumpled sample is $\mathcal{E} = \mathcal{E}_r + \mathcal{E}_c + \mathcal{E}_e$, where $\mathcal{E}_r$, $\mathcal{E}_c$ and $\mathcal{E}_e$ are the elastic energies stored in the N_r ridges, the N_c facets stacked in ordered domains and the N_e other parts of the sheet, respectively. Within a representative volume V of the sample, each of these contributions can be expressed as the sum of the N_α strain energies $e_{\alpha i}$ (per unit volume of paper) of the portions $\Omega_{\alpha i}$ of volumes $V_{\alpha i}$, of volume fractions $\phi_{\alpha i}$, with a stiffness tensor $\mathbb{C}_p$ and being subjected to a local strain field $\boldsymbol{\varepsilon}_{\alpha i}$:

$$\mathcal{E}_\alpha = \sum_{i=1}^{N_\alpha} \phi_{\alpha i} e_{\alpha i} \quad \text{with} \quad e_{\alpha i} = \frac{1}{2 V_{\alpha i}} \int_{\Omega_{\alpha i}} \boldsymbol{\varepsilon}_{\alpha i} : \mathbb{C}_p : \boldsymbol{\varepsilon}_{\alpha i} \, dV \tag{2}$$

Hence, by making the reasonable assumption that the strain energies $e_{\alpha i}$ are of the same order of magnitude, i.e., $e_{\alpha i} = \mathcal{O}(e_{\beta j})$ ($\forall \alpha, \beta, i, j$), the two following scaling expressions can be obtained:

$$\frac{\mathcal{E}_c}{\mathcal{E}_e} \approx \frac{\phi_c}{\phi_e} \quad \text{and} \quad \frac{\mathcal{E}_r}{\mathcal{E}_e} \approx \frac{\phi_r}{\phi_e} \tag{3}$$
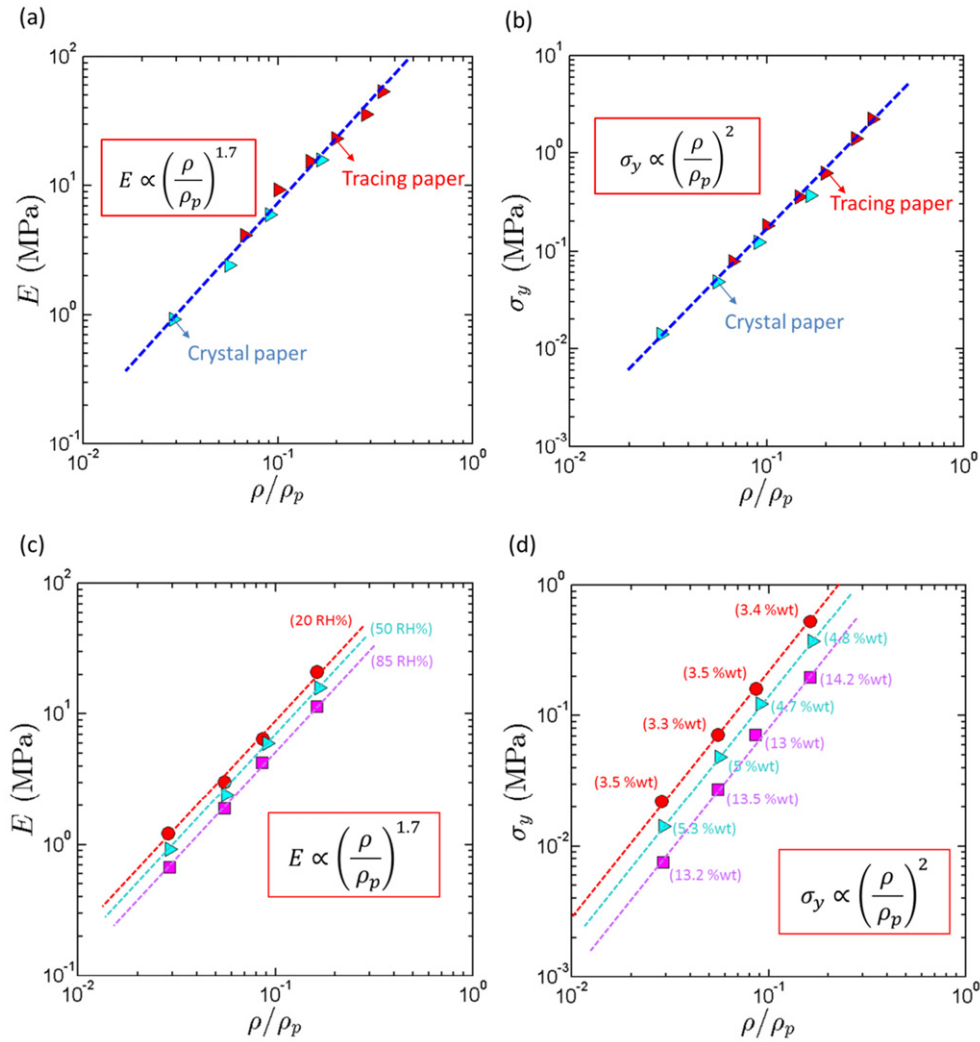
Fig. 10. Compression modulus E (a,c) and yield stress σ_y (b,d) of crumpled tracing and crystal sheets as a function of the initial relative density ρ/ρ_p. In Fig. 10c,d, the compression modulus E and the yield stress σ_y of crumpled crystal sheets is shown at different relative humidities that ranged from 20 to 80 RH%. The values in brackets shown in Fig. 10d correspond to the moisture contents.

To estimate whether the ridges, the clustered/ordered domains or the rest of the samples mainly contribute to the elastic deformation of crumpled papers, the two scaling expressions $\varepsilon_c/\varepsilon_e$ and $\varepsilon_r/\varepsilon_e$ were plotted as a function of the sheet packing fraction ρ/ρ_p using the power-laws for $\phi_c(\rho/\rho_p)$ and $\phi_r(\rho/\rho_p)$ that were previously determined from the 3D images of crumpled samples (see Figs. 7 and 8, $\phi_e = \rho/\rho_p - \phi_c - \phi_r$). The graph shown in Fig. 11 reveals that the relative contribution of ridges $\varepsilon_r/\varepsilon_e$ and ordered domains $\varepsilon_c/\varepsilon_e$ increase with the relative density of crumpled materials. The part related to ridges ε_c is minor ($\varepsilon_c < 0.1\varepsilon_e$) for relative densities lower than 0.15, of the same order of magnitude as ε_e for $\rho/\rho_p \approx 0.2$, and 10 times higher when the relative density is equal to 0.3. On the contrary, the contribution of clustered/ordered domains is more important. Indeed, ε_c is systematically higher than ε_r, of the same order as ε_e when $\rho/\rho_p \approx 0.1$, and practically 100 times higher when $\rho/\rho_p \approx 0.3$. However, it is worth noting that the conclusions drawn from this simplified analytical analysis must be taken cautiously. Further investigations, *e.g. in situ* compression tests during X-ray 3D imaging [28], and/or fine scale numerical simulations [18, 19], would be probably needed to (in)validate them.

4.2.2. Effect of sheet thickness

Crumpled materials made either with tracing or crystal papers exhibited similar scaling exponents and mechanical performances (Fig. 10a,b). Bearing in mind that both types of papers had comparable mechanical properties after moistening and drying, this suggests that the sheet thickness $\bar{t}$ has a minor effect on the mechanics of crumpled materials. Indeed, as evident from Fig. 12c,d, the normalized scaling laws $E/\overline{E}_p$ and $\sigma_y/\overline{\sigma}_{yp}$ obtained for crumpled crystal and tracing sheets could be superimposed. The analysis of 3D tomographic images showed that (i) the topology and geometry of the pattern of folds, (ii) the volume fraction of ordered domains and (iii) the geometry (thickness) of pores in both types of crumpled materials were quite comparable. Hence, the resulting similarity of the crumpling patterns led to similar scaling expressions for the elastic moduli and yield stresses: the inner structure of crumpled tracing and crystal sheets was presumably deformed in the same way during crumpling, leading to similar mechanical behaviors and scaling exponents.

4.2.3. Effect of sheet mechanical properties

As expected Fig. 10c,d show that changing the relative humidity significantly altered and decreased the compression moduli E and yield stresses σ_y of crumpled paper-based materials. In contrast, the exponents n and m of the scaling laws remained practically the same with increasing or decreasing the relative humidity. This shows that the mechanics of crumpled materials was mainly inherited from the initial
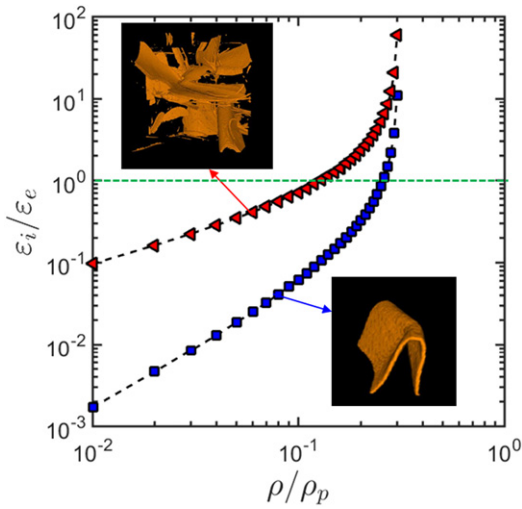
Fig. 11. Estimated evolutions of $\varepsilon_c/\varepsilon_e$ (red triangles) and $\varepsilon_r/\varepsilon_e$ (blue squares) with the relative density ρ/ρ_p.

configuration of the creased sheets. To investigate in detail the effects of the mechanical properties of the initial sheets, several crumpled aluminum foils were fabricated with various packing fractions. Then, their mechanical properties were compared with those obtained for

crumpled paper-based sheets (Fig. 12). Crumpled aluminum materials exhibited higher compression modulus E than crumpled crystal and tracing sheets. This clearly shows the role of the mechanical properties of the initial sheets on the mechanical performances of crumpled structures: aluminum sheets had higher mean Young's modulus $\overline{E}_p$ than tracing and crystal sheets, resulting in higher compression moduli E for the crumpled aluminum materials. A similar remark can be drawn for the yield stress σ_y: crumpled aluminum and paper-based materials exhibited similar yield stresses $\overline{\sigma}_{yp}$ as the initially flat aluminum and paper sheets had comparable yield stress $\overline{\sigma}_{yp}$ (≈ 50 MPa).

However, similarly to crumpled paper-based materials, E and σ_y for aluminum based materials were both power-law functions of ρ/ρ_p, with similar power-law exponents $n \approx 1.7$ and $m \approx 2$. These scaling exponents are different from those reported by Bouaziz et al. [8] ($n = 2.4$ and $m = 1.7$) and Balankin et al. [10] ($n = 1.5$ and $m = 0.9$). This discrepancy probably results from the fabrication conditions of the samples that might have induced different folded microstructures.

Fig. 12c,d also show that crumpled aluminum and paper-based materials exhibited practically the same normalized scaling laws $E/\overline{E}_p$ and $\sigma_y/\overline{\sigma}_{yp}$. This would indicate that both crumpled materials have similar folded microstructures. However, Tallinen et al. [19], showed, using numerical simulation, that the folded configuration, namely the geometry of the pattern of ridges formed during crumpling, was affected by the intrinsic mechanical characteristics of the initial sheets. Here, the similarities between both types of crumpled materials, made either of aluminum or papers, could be related to the 'plasticization' of paper sheets before crumpling because of the moistening pre-treatment.
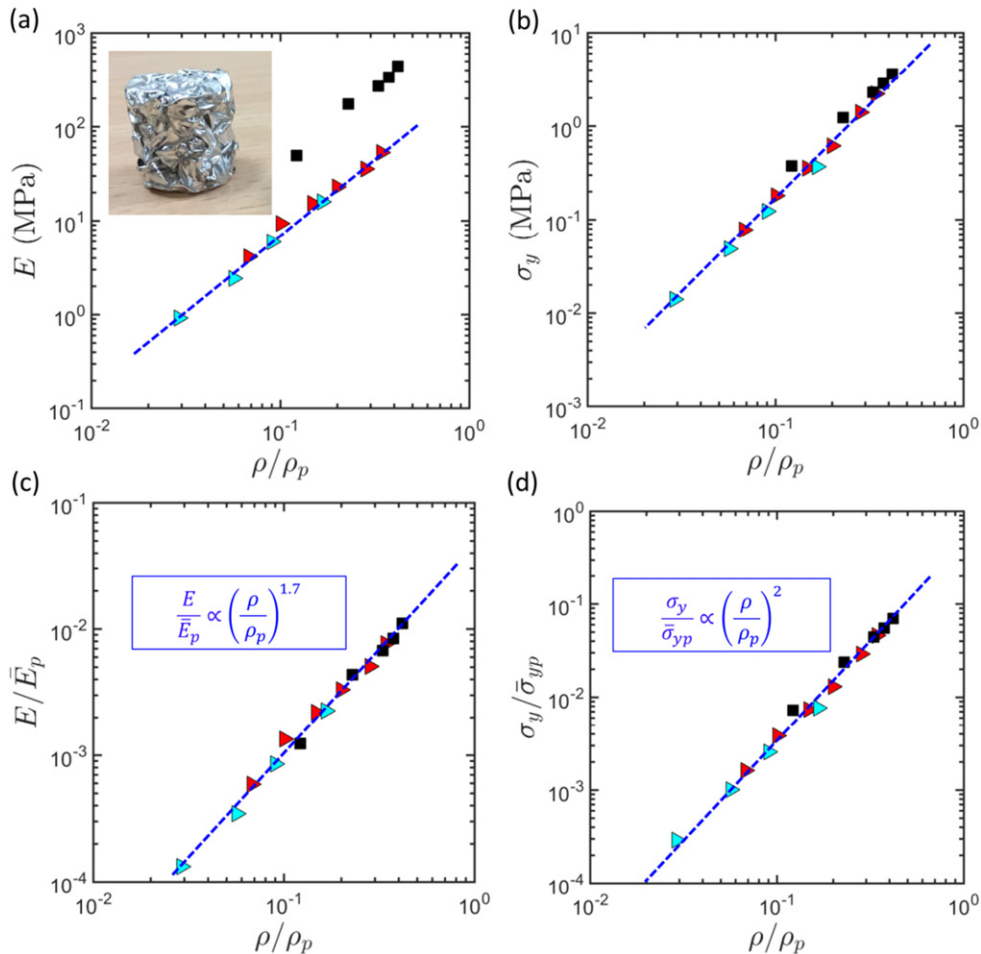

Fig. 12. Compression moduli E (a) and yield stresses σ_y (b) of crumpled paper (triangle symbols) and aluminum (black square symbols) sheets as functions of the initial relative density ρ/ρ_p. In Fig. 12c,d, E and σ_y were normalized by the mean elastic moduli $\overline{E}_p$ and yield stresses $\overline{\sigma}_{yp}$ of the initial sheets (Fig. 1).

This pre-treatment lowers the elastic properties and confers prominent plastic ductile behavior to the initial paper sheets that is similar to that of aluminum foils. Note also that the moistened paper sheets do no undergo pronounced strain relaxation after demolding, as it can be observed for randomly folded aluminum foils.

Finally, the strong similarities in the scaling laws observed for elastoplastic aluminum and paper sheets indicate that the combined deformation micro-mechanisms of the crumpling networks are material-independent, thus leading to similar scaling exponents n and m.

4.3. Comparison with classical cellular materials

In Fig. 13, the mechanical performances of crumpled paper-based materials with different relative densities were plotted in Ashby-type materials selection charts [1,14] and compared with those of commercially-available foams of similar densities. Keeping in mind their very low fabrication cost, this new class of biobased cellular materials with only self-locking architectures is rather well-positioned in the graphs:

- Crumpled papers exhibit mechanical performances between those of flexible and rigid commercially-available polymer foams that are widely used in many engineering applications.
- They also have higher specific mechanical properties in comparison with other cellulosic foams such as, for instance, cellulose nanofibril foams [28] that are prepared by freeze-casting or ice-templating.
- Compared to crumpled aluminum sheets, crumpled papers exhibit much higher specific yield stresses and have similar elastic properties. They also show noticeable strain recovery upon unloading that could be interesting for cushioning applications.

In addition, it is also worth noting that the strength and stiffness of crumpled materials could be considerably improved. Indeed, the surface of the uncrumpled sheets could be coated with a bonding material (e.g., elastomers, rubbers, starch etc.) which would allow self-contacts of crumpled sheets to exhibit cohesion [9,47].

Hence, combined with their low-cost and easy fabrication, it is clear that crumpled papers constitute promising solutions for several engineering applications. They could be used to replace synthetic foams in many applications requiring cost reduction (for example in packaging [47,48]) or even to substitute honeycomb materials that are widely used in sandwich panels, owing to their more isotropic architecture and presumably highest in-plane lateral compression or transverse shear resistances. These materials are also potentially relevant design solutions for many engineering applications requiring high impact resistance and energy absorption. Indeed, materials with self-locked architectures are prone to exhibit remarkable damping capacity because of the increased frictional mechanisms occurring in the numerous contacts distributed in the 3D structure [3,4,11].

Eventually, the fabrication method presented in this study is versatile enough to tune easily the process-induced architectures. For example, by changing the initial length of the papers or the compaction rate [11], samples with different porosities, anisotropies and mechanical properties can be obtained. In addition, a simple scaling of the sheet thickness enables the pore size distribution to be tailored. Parts with large dimensions could be obtained using industrial compression molding processes commonly used in manufacturing thermoset plastic or composite parts [49] or even paper crumpling machines already used in the industry for producing packaging cushioning. More elaborated structures could also be fabricated through the assembly of individually interlocking smaller-shaped subunits [50].

5. Conclusion

This study shows that paper sheets can be used to easily obtain lightweight porous materials with interesting architectures and mechanical
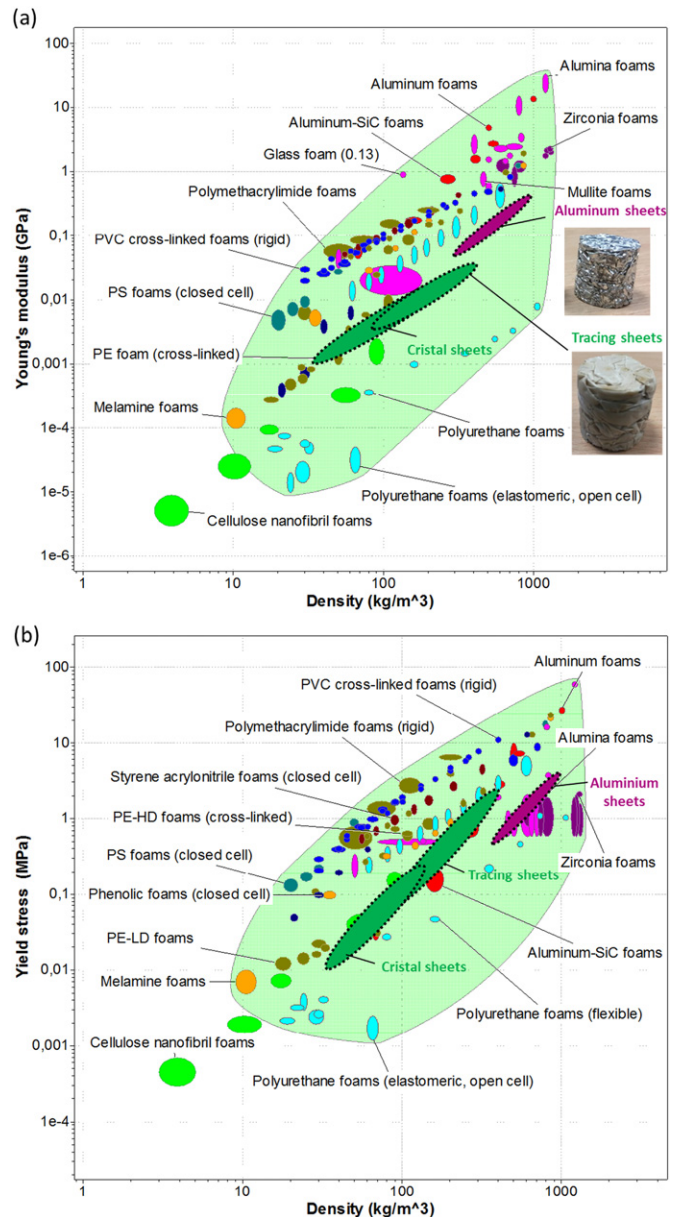

Fig. 13. Elastic modulus E (a) and yield stress σ_y (b) as functions of density ρ for the studied crumpled paper-based materials and some commercially-available polymer foams [1,14].

properties, only by crumpling them. The simple and versatile fabrication route used in this study allows biobased solid cellular materials with controlled geometry and sizes to be obtained. It consists in moistening the initial paper sheets before crumpling and then drying them inside a cylindrical die to avoid paper relaxation after demolding. The as-prepared samples exhibited isotropic self-locked architectures. Using X-ray microtomography, the process-induced microstructures of the materials was finely characterized. Their inner structure consisted of an assembly of interacting folds and interlocked thin facets. Several clustered and ordered domains within which the sheets were stacked in layers were also formed in the bulk of the materials during crumpling.

Crumpled papers exhibit reproducible compression behavior that is typical of many elastoplastic cellular materials, i.e., with successive linear, strain-hardening and densification regimes. Both the yield stress and the elastic moduli were power-law functions of the relative density. The scaling exponents indicated that the compression behavior of crumpled structures could result from multiple combined deformation

mechanisms such as bending of the ridges and bending and stretching of multiple interlocked thin facets. The numerous layered stacks that are present in the crumpled structures could also contribute in a complex manner to the mechanical rigidity of the systems. A simple micromechanical analysis was carried out to estimate the effect of ridges and ordered domains on the mechanical properties of crumpled papers. However, to better understand the mechanics of crumpled materials and the role of the crumpled architecture, 3D *in situ* compression tests during real time X-ray microtomography imaging could be performed [28].

These preliminary results show that these low-cost and easy processable materials exhibit mechanical properties that are comparable with flexible and rigid commercially-available polymer or aluminum foams of similar densities. Thus, they constitute promising solutions for several engineering applications. For example, they could be used as core materials in sandwich panels because of their promising shock absorbing and cushioning properties or as insulating materials because of the low thermal conductivity of paper sheets.

Acknowledgements

References

[1] L.J. Gibson, M.F. Ashby, Cellular Solids: Structure and Properties, Cambridge University Press, 1999.
[2] N. Mills, Polymer Foams Handbook: Engineering and Biomechanics Applications and Design Guide, Butterworth-Heinemann, 2007.
[3] B. Gadot, O. Riu Martinez, S. Rolland du Roscoat, D. Bouvard, D. Rodney, L. Orgéas, Entangled single-wire NiTi material: a porous metal with tunable superelastic and shape memory properties, Acta Mater. 96 (2015) 311–323.
[4] D. Rodney, B. Gadot, O.R. Martinez, S.R. du Roscoat, L. Orgéas, Reversible dilatancy in entangled single-wire materials, Nat. Mater. 24 (2016) 72–77.
[5] M.F. Ashby, The properties of foams and lattices, Philos. Trans. R. Soc. Lond. Math. Phys. Eng. Sci. 364 (2006) 15–30.
[6] B. Honig, Protein folding: from the levinthal paradox to structure prediction, J. Mol. Biol. 293 (1999) 283–293.
[7] E. Tejera, A. Machado, I. Rebelo, J. Nieto-Villar, Fractal protein structure revisited: topological, kinetic and thermodynamic relationships, Phys. Stat. Mech. Appl. 388 (2009) 4600–4608.
[8] O. Bouaziz, J.P. Masse, S. Allain, L. Orgéas, P. Latil, Compression of crumpled aluminum thin foils and comparison with other cellular materials, Mater. Sci. Eng. A 570 (2013) 1–7.
[9] S. Cottrino, P. Viviès, D. Fabrègue, E. Maire, Mechanical properties of crumpled aluminum foils, Acta Mater. 81 (2014) 98–110.
[10] A.S. Balankin, M.A.M. Cruz, L.A.A. Caracheo, O.S. Huerta, C.D. Rivas, C.L. Martínez, D.S. Ochoa, L.M. Ruiz, S.M. Gutiérrez, J.P. Ortiz, M.P. Ortiz, Mechanical properties and relaxation behavior of crumpled aluminum foils, J. Mater. Sci. 50 (2015) 4749–4761.
[11] D.A.H. Hanaor, E.A. Flores Johnson, S. Wang, S. Quach, K.N. Dela-Torre, Y. Gan, L. Shen, Mechanical properties in crumple-formed paper derived materials subjected to compression, Heliyon 3 (2017).
[12] R.C. Picu, Mechanics of random fiber networks—a review, Soft Matter 7 (2011) 6768–6785.
[13] M. Habibi, M. Adda-Bedia, D. Bonn, Effect of the material properties on the crumpling of a thin sheet, Soft Matter 13 (2017) 4029–4034.
[14] M.F. Ashby, Materials Selection in Mechanical Design, 4 edition Butterworth-Heinemann, Burlington, MA, 2010.
[15] A.J. Wood, Witten's lectures on crumpling, Phys. Stat. Mech. Appl. 313 (2002) 83–109.
[16] M.A.F. Gomes, T.I. Jyh, T.I. Ren, I.M. Rodrigues, C.B.S. Furtado, Mechanically deformed crumpled surfaces, J. Phys. D. Appl. Phys. 22 (1989) 1217.
[17] A.S. Balankin, A.H. Rangel, G.G. Pérez, F.G. Martinez, H.S. Chavez, C.L. Martínez-González, Fractal features of a crumpling network in randomly folded thin matter and mechanics of sheet crushing, Phys. Rev. E 87 (2013) 052806.
[18] G.A. Vliegenthart, G. Gompper, Forced crumpling of self-avoiding elastic sheets, Nat. Mater. 5 (2006) 216–221.
[19] T. Tallinen, J.A. Aström, J. Timonen, The effect of plasticity in crumpling of thin sheets, Nat. Mater. 8 (2009) 25–29.
[20] A.S. Balankin, O.S. Huerta, Fractal geometry and mechanics of randomly folded thin sheets, IUTAM Symp. Scaling Solid MechSpringer 2009, pp. 233–241.
[21] A.S. Balankin, D.S. Ochoa, I.A. Miguel, J.P. Ortiz, M.Á.M. Cruz, Fractal topology of hand-crumpled paper, Phys. Rev. E 81 (2010), 061126.
[22] A.D. Cambou, N. Menon, Three-dimensional structure of a sheet crumpled into a ball, Proc. Natl. Acad. Sci. 108 (2011) 14741–14745.
[23] A.D. Cambou, N. Menon, Orientational ordering in crumpled elastic sheets, EPL Europhys. Lett. 112 (2015) 14003.
[24] Y.-C. Lin, J.-M. Sun, H.W. Yang, Y. Hwu, C.L. Wang, T.-M. Hong, X-ray tomography of a crumpled plastoelastic thin sheet, Phys. Rev. E 80 (2009), 066114.
[25] Y.-C. Lin, J.-M. Sun, J.-H. Hsiao, Y. Hwu, C.L. Wang, T.-M. Hong, Spontaneous emergence of ordered phases in crumpled sheets, Phys. Rev. Lett. 103 (2009) 263902.
[26] D.L. Blair, A. Kudrolli, Geometry of crumpled paper, Phys. Rev. Lett. 94 (2005).
[27] K. Niskanen, Mechanics of Paper Products, Walter de Gruyter, 2012.
[28] F. Martoïa, T. Cochereau, P.J.J. Dumont, L. Orgéas, M. Terrien, M.N. Belgacem, Cellulose nanofibril foams: links between ice-templating conditions, microstructures and mechanical properties, Mater. Des. 104 (2016) 376–391.
[29] M.A. Beltran, D.M. Paganin, K. Uesugi, M.J. Kitchen, 2D and 3D X-ray phase retrieval of multi-material objects using a single defocus distance, Opt. Express 18 (2010) 6423–6436.
[30] D. Paganin, S.C. Mayo, T.E. Gureyev, P.R. Miller, S.W. Wilkins, Simultaneous phase and amplitude extraction from a single defocused image of a homogeneous object, J. Microsc. 206 (2002) 33–40.
[31] N. Otsu, A threshold selection method from gray-level histograms, IEEE Trans. Syst. Man Cybern. 9 (1979) 62–66.
[32] C.A. Schneider, W.S. Rasband, K.W. Eliceiri, NIH Image to ImageJ: 25 years of image analysis, Nat. Methods 9 (2012) 671.
[33] T.P. Harrigan, R.W. Mann, Characterization of microstructural anisotropy in orthotropic materials using a second rank tensor, J. Mater. Sci. 19 (1984) 761–767.
[34] M. Doube, M.M. Klosowski, I. Arganda-Carreras, F.P. Cordelières, R.P. Dougherty, J.S. Jackson, B. Schmid, J.R. Hutchinson, S.J. Shefelbine, BoneJ: free and extensible bone image analysis in ImageJ, Bone 47 (2010) 1076–1079.
[35] N.L. Fazzalari, I.H. Parkinson, Fractal dimension and architecture of trabecular bone, J. Pathol. 178 (1996) 100–105.
[36] E. Maire, P. Colombo, J. Adrien, L. Babout, L. Biasetto, Characterization of the morphology of cellular ceramics by 3D image processing of X-ray tomography, J. Eur. Ceram. Soc. 27 (2007) 1973–1981.
[37] V. Boulos, V. Fristot, D. Houzet, L. Salvo, P. Lhuissier, Investigating performance variations of an optimized GPU-ported granulometry algorithm, Des. Archit. Signal Image Process. DASIP 2012 Conf. onIEEE 2012, pp. 1–6.
[38] J.B. Brzoska, B. Lesaffre, C. Coléou, K. Xu, R.A. Pieritz, Computation of 3D curvatures on a wet snow sample, Eur. Phys. J. Appl. Phys. 7 (1999) 45–57.
[39] Y. Nishikawa, T. Koga, T. Hashimoto, H. Jinnai, Measurements of interfacial curvatures of bicontinuous structure from three-dimensional digital images. 2. A sectioning and fitting method, Langmuir 17 (2001) 3254–3265.
[40] H. Pottmann, J. Wallner, Q.-X. Huang, Y.-L. Yang, Integral invariants for robust geometry processing, Comput. Aided Geom. Des. 26 (2009) 37–60.
[41] D. Coeurjolly, J.-O. Lachaud, J. Levallois, Multigrid convergent principal curvature estimators in digital geometry, Comput. Vis. Image Underst. 129 (2014) 27–41.
[42] F. Flin, J.-B. Brzoska, B. Lesaffre, C. Coléou, R.A. Pieritz, Three-dimensional geometric measurements of snow microstructural evolution under isothermal conditions, Ann. Glaciol. 38 (2004) 39–44.
[43] J.A. Sethian, Level set methods and fast marching methods: evolving interfaces in computational geometry, fluid mechanics, computer vision, and materials science, Cambridge university press, 1999.
[44] F. Flin, J.-B. Brzoska, D. Coeurjolly, R.A. Pieritz, B. Lesaffre, C. Coleou, P. Lamboley, O. Teytaud, G.L. Vignoles, J.-F. Delesse, Adaptive estimation of normals and surface area for discrete 3-D objects: application to snow binary data from X-ray tomography, IEEE Trans. Image Process. 14 (2005) 585–596.
[45] W.W. Sampson, Modelling Stochastic Fibrous Materials with Mathematica®, Springer Science & Business Media, 2008.
[46] A.P. Philipse, S.G. Kluijtmans, Sphere caging by a random fibre network, Phys. Stat. Mech. Appl. 274 (1999) 516–524.
[47] Weder D. Packaging material, U.S. patent 5,196,043, Jun. 8, 1999.
[48] Cheich C. Robert. Cohesive Packaging Material in a Shipping Container and Method, U.S. patent 2008/0210591, Sep. 4, 2008.
[49] L. Orgéas, P.J. Dumont, Sheet molding compounds, Wiley Encycl. Compos, 2012.
[50] M. Dugue, M. Fivel, Y. Bréchet, R. Dendievel, Indentation of interlocked assemblies: 3D discrete simulations and experiments, Comput. Mater. Sci. 79 (2013) 591–598.